1
2
3
4
5
6
7
8
9
10
11
12
13
14
15
16
17
18
19
20
21
22
23
24
25
26
27
28
29
30
31
32
33
34
35
36
37
38
39
40
41
42
43
44
45
46
47
48
49
50
51
52
53
54
55
56
57
58
59
60

Dynamic electro-thermo-mechanical modeling of a U-shaped electrothermal actuator

Hussein Hussein, Aref Tahhan, Patrice Le Moal, Gilles Bourbon, Yassine Haddab and Philippe Lutz

Femto-st Institute, Besancon, France

E-mail: `hussein.hussein@femto-st.fr`

October 2015

Abstract. In this paper, we develop original analytical electro-thermal and thermo-mechanical models for the U-shaped electrothermal actuator. Dynamics of the temperature distribution and displacement are obtained as a direct relationship between the system dimensions, material properties and electrical input.

The electrothermal model provides an exact solution of the hybrid PDEs that describe the electrothermal behavior for each of the actuator's three connected arms. The solution is obtained using a new calculation method that allows representing an integrable function by an hybrid infinite sum of sine and cosine functions. Displacement at the actuator's tip is then calculated using a quasi-static model based on the superposition and virtual works principles.

Obtained temperature and displacement solutions are then discussed and compared with finite element method (FEM) simulations via ANSYS and experimental results. Comparisons showed good agreement making the proposed modeling a reliable alternative which paves the way for improving the design and optimizing the dimensions of U-shaped micro-actuators.

Keywords: U-shaped actuator, electrothermal, thermomechanical, modeling, MEMS

Submitted to: *J. Micromech. Microeng.*

2

1. INTRODUCTION

A U-Shaped electrothermal actuator is a series of three connected lineshaped beams (hot arm, cold arm and flexure), in a folded configuration as can be seen in figure 1.

The electrothermal heating of different arms with variable sections leads to non-equivalent expansions between the two sides of the folded actuator. The slight expansion of those arms is amplified by the structure to generate a considerable displacement at the tip of the actuator.
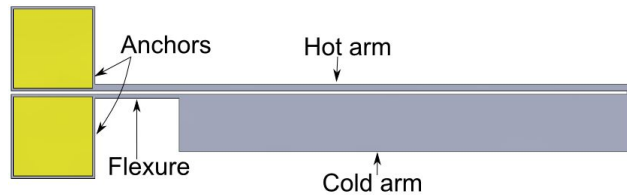

Figure 1. U-shaped electrothermal micoractuator.

The U-shaped actuator can output high forces with a wide range of displacement compared to other microactuators in MEMS. It has a repeatable behavior, long life time [1], small footprint, simple design, and tolerance to working conditions (dust, moisture...). Its monolithic single material structure makes it compliant with standard MEMS-based fabrication processes.

This design, firstly introduced in 1992 [2], is being widely exploited during the last two decades especially in MEMS applications [3, 4, 5, 6, 7, 8] due to its obvious advantages which pushed research towards ameliorating the design and the performance of the actuator.

Modeling the behavior of the actuator is a diverse task since it is an interaction of several domains : electricity, thermal distribution, structural expansion and elastic deformation. Usually, the modeling process is a sequence of two models: Electro-thermal and thermo-mechanical. The first one allows computing the temperature values at each section as a result of joule heating, the second one estimates the displacement at the actuator's tip according to the obtained temperature distribution.

Numerous electrothermal [9, 10, 11, 12, 13] and thermomechanical [9, 11, 12, 13] models have been presented in previous works on the U-shaped actuator, yet few studies [13, 14, 15, 16, 17, 18] are found that have addressed the dynamic response of the U-shaped actuator. Further, experiments and simulations in our previous work [18] showed a dynamic behavior that is related to the thermal dynamic while the elastic response is quasistatic relatively. Therefore, dynamic electrothermal model and static thermomechanical model are required.

An analytical formulation of the steady state and transient solutions of the electrothermal response of a lineshaped beam are presented in [19]. As for the U-shaped actuator, the steady state solution was investigated in [20]. As for the transient solution, the problem was solved numerically in [13] using Laplace transformation.

As far as we know, no exact analytical solution of the transient electrothermal response of the actuator was found in literature. In the case of a simple beam, solving the electrothermal equation revolves around the recognition of a Fourier series form of the general solution after introducing boundary and initial conditions (Appendix A). This is not the case for the U-shaped actuator.

The difficulty in the case of the actuator lies in the fact that the arms are differently heated, and temperature evolution in each arm is described by an equation. This leads to a general solution in the form of a hybrid function with three sub-functions, each one concerns one arm of the actuator. In result, the hybrid function cannot be recognized as a Fourier series, and no solution can be obtained with this method.

An exact analytical solution of the electrothermal problem of the actuator is presented in this paper using a novel calculation method that allows presenting an integrable function by a hybrid function, where sub-functions consist of infinite sum of sines and cosines. Expression of the temperature final solution is an infinite sum of periodic functions where all the parameters are determined. This analytical expression describes evolution of the temperature distribution inside the actuator in response to an electrical input.

As for the thermo-mechanical model, in previous works, several approaches were considered to estimate the displacement at the tip using mainly the length thermal expansion in each arm. The difference of enthalpy approach was used in [12], Castiglianos theory approach as in [16] and Euler-Bernoulli equation was derived to estimate the displacement in [21]. As in the validated model [20] where the virtual works method was used, in our proposed model we calculate the displacement using the same method but we have chosen not to make any of the simplifications done previously in order to obtain a solution of a more general case with regard to the dimensions of the actuator.

The importance of the proposed models, lies not only in the estimation of the displacement and temperature distribution; but also to their capability of showing the effects of different parameters and dimensions on the response, a key tool for the design and optimization.

The models and solutions will be addressed in the following sections, the actuator's electrothermal

new solution is presented followed by the thermo-mechanical modeling. Finally, analytical solutions are discussed and compared to FEM modeling and experimental results. Calculation method of the electrothermal equation for a lineshaped structure is recalled in Appendix A.

2. Electrothermal modeling of the actuator

2.1. Electrothermal equation

At the microscale, the heat transfer mechanisms are different from the macroscale [22, 23]. Conduction is dominant on the free convection [23] while radiation is negligible as in several previous studies [9, 10, 11]. As for, conduction should be treated as the only mode of heat transfer in the absence of forced convection and radiation [23].

The models for the U-shaped actuator are generally one dimensional and have simplifying assumptions. The temperature is considered to be uniform in the cross section for microactuators [5, 24].

In this paper, convection and radiation effects are then neglected in the electrothermal modeling and a one dimensional simplification is considered making the device modeled unfolded. So, with regards to the previous, the electrothermal partial differential equation (PDE) that allows describing the temperature T in terms of the space dimension x and time t is as follows:

$$\rho_d C_p \frac{\partial T}{\partial t} = J^2 \rho_0 + K_p \frac{\partial^2 T}{\partial x^2} \tag{1}$$

ρ_d: density in $\frac{kg}{m^3}$
C_p: specific heat in $\frac{J}{K.kg}$
J: electrical current density in $\frac{A}{m^2}$
ρ_0: electrical resistivity in $\Omega.m$
K_p: thermal conductivity in $\frac{W}{K.m}$

The term on the left of (1) represents the density of heat added due to thermal variation. The first term on the right represents the heat generation by Joule effect, the one next concerns the conduction between sections and the anchors.

2.2. Actuator electrothermal response

In this section, we model the system using three electrothermal PDEs that are continuous in temperature and heat flux density, one for each arm of the actuator.

The folded actuator (figure 1) is modeled unfolded in order to match the one dimension 1D hypothesis. Coordinates and dimensions of the actuator are shown in figure 2.
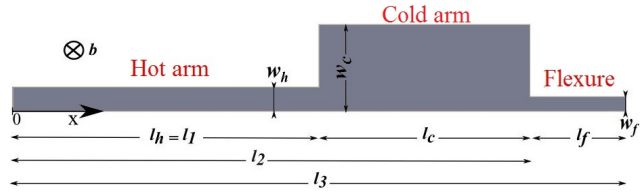

Figure 2. Unfolded actuator

The temperature distribution $T(x,t)$ in the case of the actuator is a hybrid function with three sub-functions that represent the temperature in each of the three arms.

$$T(x,t) = \begin{cases} T_h(x,t) & x \in [0;l_1] \\ T_c(x,t) & x \in [l_1;l_2] \\ T_f(x,t) & x \in [l_2;l_3] \end{cases} \tag{2}$$

Where the indexes h, c and f refer to the hot arm, cold arm and flexure respectively.

In order to simplify the presentation of the model, the index k refers to the three different arms as follows:

$$\{eq._k\} \equiv \begin{cases} eq._{k\equiv h} & x \in [0;l_1] \\ eq._{k\equiv c} & x \in [l_1;l_2] \\ eq._{k\equiv f} & x \in [l_2;l_3] \end{cases} \tag{3}$$

Three different equations allow defining the electrothermal behavior of each arm taking in consideration the thermal exchanges in all three as follows:

$$\left\{ \frac{\partial^2 T_k}{\partial x^2} = \frac{1}{\alpha_p} \frac{\partial T_k}{\partial t} - \frac{J_k^2 \rho_0}{K_p} \right\} \tag{4}$$

The steady state temperature solution (T_{ss}) has the following distribution in all three arms:

$$\left\{ T_{kss}(x) = -\frac{J_k^2 \rho_0}{2K_p} x^2 + d_{k1} x + d_{k2} \right\} \tag{5}$$

Where d_{h1}, d_{h2}, d_{c1}, d_{c2}, d_{f1} and d_{f2} are constants.

In addition to the boundary conditions at both ends of the actuator, there are also continuity conditions between adjacent arms in temperature and heat flux density. Considering the boundary and continuity conditions allows determining the values of d_{k1} and d_{k2} in (5):

$$\begin{array}{ll} T_h(0,t) = T_\infty & T_f(l_3) = T_\infty \\ T_h(l_1,t) = T_c(l_1,t) & A_h \frac{\partial T_1}{\partial x}(l_1,t) = A_c \frac{\partial T_c}{\partial x}(l_1,t) \\ T_c(l_2,t) = T_f(l_2,t) & A_c \frac{\partial T_c}{\partial x}(l_2,t) = A_f \frac{\partial T_f}{\partial x}(l_2,t) \end{array} \tag{6}$$

Where A_h, A_c and A_f are the arms section areas, and T_∞ is the ambient temperature.

As in the lineshaped beam case (Appendix A), the transient solution of temperature is a sum of the steady state temperature solution and a sum of separated variable function as follows :

$$\left\{ T_k(x,t) = T_{kss}(x) + \sum_{n=1}^{\infty} X_{kn}(x) T_{kn}(t) \right\} \tag{7}$$

4

The general solutions of $T_{kn}(t)$ and $X_{kn}(x)$ have the following forms (Appendix A):

$$\left\{ \begin{array}{l} T_{kn}(t) = e^{-\alpha_p \lambda_n^2 t} \\ X_{kn}(x) = a_{kn}\sin(\lambda_n x) + b_{kn}\cos(\lambda_n x) \\ \qquad\quad = C_{kn}\sin(\lambda_n x + \varphi_{kn}) \end{array} \right\} \qquad (8)$$

Introducing the boundary and continuity conditions in (6) leads to the following conditions on X_{kn}:

$$\begin{array}{ll} X_{hn}(0) = 0 & X_{fn}(l_3) = 0 \\ X_{hn}(l_1) = X_{cn}(l_1) & A_h\frac{\partial X_{hn}}{\partial x}(l_1) = A_c\frac{\partial X_{cn}}{\partial x}(l_1) \\ X_{cn}(l_2) = X_{fn}(l_2) & A_c\frac{\partial X_{cn}}{\partial x}(l_2) = A_f\frac{\partial X_{fn}}{\partial x}(l_2) \end{array} \qquad (9)$$

Applying the conditions in (9) on X_{kn} allows obtaining the equation of λ_n and defining the relation between a_{hn} and the other constants. The relations between a_{hn} and the other constants are as follows:

$$\begin{aligned} b_{hn} &= 0 \\ \frac{b_{cn}}{a_{hn}} &= \left(1 - \frac{A_h}{A_c}\right)\sin(\lambda_n l_h)\cos(\lambda_n l_h) \\ \frac{a_{cn}}{a_{hn}} &= \sin^2(\lambda_n l_h) + \frac{A_h}{A_c}\cos^2(\lambda_n l_h) \\ \frac{b_{fn}}{a_{hn}} &= -\frac{a_{fn}}{a_{hn}}\tan(\lambda_n l_3) \\ \frac{a_{fn}}{a_{hn}} &= \cos(\lambda_n l_c)\left(\begin{array}{l} \frac{A_h}{A_f}\cos(\lambda_n l_2)\cos(\lambda_n l_1) \\ + \sin(\lambda_n l_2)\sin(\lambda_n l_1) \end{array}\right) \\ &\quad + \sin(\lambda_n l_c)\left(\begin{array}{l} \frac{A_h}{A_c}\sin(\lambda_n l_2)\cos(\lambda_n l_1) \\ - \frac{A_c}{A_f}\cos(\lambda_n l_2)\sin(\lambda_n l_1) \end{array}\right) \end{aligned} \qquad (10)$$

In addition, the equation of λ_n concluded from (9) is as follows:

$$\begin{aligned} &A_h A_c \cos(\lambda_n l_h)\cos(\lambda_n l_c)\sin(\lambda_n l_f) + \\ &A_h A_f \cos(\lambda_n l_h)\sin(\lambda_n l_c)\cos(\lambda_n l_f) + \\ &A_c A_f \sin(\lambda_n l_h)\cos(\lambda_n l_c)\cos(\lambda_n l_f) - \\ &A_c^2 \sin(\lambda_n l_h)\sin(\lambda_n l_c)\sin(\lambda_n l_f) = 0 \end{aligned} \qquad (11)$$

Unlike the case of a lineshaped beam, the trigonometric equation (11) doesn't allow obtaining a simple analytical form of λ_n. The values of λ_n for the actuator must be then calculated numerically using (11).

Yet, a kind of periodicity for the values of λ_n is noticed. If the total length of the arms can be written as a positive integer after scaling, then λ_{K_l} is the K_lth solution of λ_n:

$$\lambda_{K_l} = \frac{K_l \pi}{l_3} \qquad (12)$$

K_l is a least common multiple (lcm) between lengths of arms:

$$K_l = lcm\left(\frac{lcm(l_h, l_3)}{l_h}, \frac{lcm(l_c, l_3)}{l_c}, \frac{lcm(l_f, l_3)}{l_f}\right) \qquad (13)$$

In result, the solutions of λ_n are periodic as follows:

$$\lambda_{K_l + n} = \lambda_{K_l} + \lambda_n \qquad (14)$$

In our case, $l_3 = 2l_h$, then the first part in (13) is equivalent to 2 and K_l is always an even number. In this case, $\lambda_{K_l/2} = (K_l \pi)/(2l_3)$ is also a solution of λ_n. The first K_l solutions of λ_n are also symmetric as follows:

$$\lambda_{K_l - n} = \lambda_{K_l} - \lambda_n \qquad (15)$$

Therefore, it is sufficient to calculate only the first λ_n solutions for $\lambda_n \leq (K_l \pi)/(2l_3)$. The other λ_n are defined by symmetry and periodicity.

Returning to the modeling, the second representation of $X_{kn}(x)$ in (8) with C_{kn}, λ_n and φ_{kn} is adopted in order to present the developed solution hereinafter:

$$\begin{aligned} C_{kn} &= \sqrt{a_{kn}^2 + b_{kn}^2} \\ \varphi_{kn} &= \left\{ \begin{array}{ll} -\tan^{-1}\left(\frac{b_{kn}}{a_{kn}}\right) & a_{kn} > 0 \\ \pi - \tan^{-1}\left(\frac{b_{kn}}{a_{kn}}\right) & a_{kn} < 0 \end{array} \right. \end{aligned} \qquad (16)$$

The values of φ_{kn} can be concluded from (10) and (16). The relations of C_{cn}, C_{fn} with respect to C_{hn} are as follows:

$$\begin{aligned} C_{hn} &= |a_{hn}| \\ \frac{C_{cn}}{C_{hn}} &= \left| \begin{array}{l} \frac{A_h}{A_c}\sin^2(\lambda_n l_h) + \cos^2(\lambda_n l_h) \\ + \left(\frac{A_h}{A_c} - 1\right)\sin(\lambda_n l_h)\cos(\lambda_n l_h) \end{array} \right| \\ \frac{C_{fn}}{C_{hn}} &= \left| \frac{a_{fhn}}{\cos(\lambda_n l_3)} \right| \end{aligned} \qquad (17)$$

Among the 7 unknown constants in (8), λ_n is obtained from (11) and all others are defined according to only one constant C_{hn} (17). This constant can be calculated by introducing the initial distribution of temperature:

$$\left\{ \sum_{n=1}^{\infty} C_{kn}\sin(\lambda_n x + \varphi_{kn}) = T_{k_0}(x) - T_{k_{ss}}(x) \right\} \qquad (18)$$

The recognition of a Fourier series allows calculating the unknown constants in the case of a lineshaped beam (Appendix A). Fourier series allows representing any integrable function by an infinite sum of sine waves. The sine waves are periodic on a determined range while the sine and cosine constants are continuous throughout the period.

These conditions are satisfied in the case of the lineshaped beam, while the hybrid and aperiodic nature of the temperature distribution along the actuator prevents the application of the same principle for calculating the constants of the actuator electrothermal response.

A solution for the unknown constant in (18) is presented in the following using a novel calculation method to present an integrable function by a sum of hybrid sine and cosine functions. In order to calculate the values of the constants C_h, C_c, C_f, φ_h, φ_c and φ_f that correspond to $\lambda_n = \lambda$, we multiply the first row in (18) by $C_h A_h \sin(\lambda x + \varphi_h)$, the second row by

$C_c A_c \sin(\lambda x + \varphi_c)$ and the third row by $C_f A_f \sin(\lambda x + \varphi_f)$ and integrate the result over the length of the actuator:

$$\int_0^{l_3} \sum_{n=1}^{\infty} \left\{ \begin{array}{c} C_{kn} C_k A_k \sin(\lambda_n x + \varphi_{kn}) \\ \cdot \sin(\lambda x + \varphi_k) \end{array} \right\} dx$$
$$= \int_0^{l_3} \left\{ C_k A_k \left(T_{k_0}(x) - T_{k_{ss}}(x) \right) \sin(\lambda x + \varphi_k) \right\} dx \qquad (19)$$

Noting that:

$$\int_0^{l_3} \{eq._k\} dx =$$
$$\int_0^{l_1} eq._{k \equiv h} dx + \int_{l_1}^{l_2} eq._{k \equiv c} dx + \int_{l_2}^{l_3} eq._{k \equiv f} dx \qquad (20)$$

The first side in (19) can be decomposed in two parts:

$$\int_0^{l_3} \sum_{n=1}^{\infty} \left\{ \begin{array}{c} C_{kn} C_k A_k \sin(\lambda_n x + \varphi_{kn}) \\ \cdot \sin(\lambda x + \varphi_k) \end{array} \right\} dx$$
$$= \int_0^{l_3} \sum_{\lambda_n \neq \lambda} \left\{ \begin{array}{c} C_{kn} C_k A_k \sin(\lambda_n x + \varphi_{kn}) \\ \cdot \sin(\lambda x + \varphi_k) \end{array} \right\} dx \qquad (21)$$
$$+ \int_0^{l_3} \left\{ C_k^2 A_k \sin^2(\lambda x + \varphi_k) \right\} dx$$

Considering boundary and continuity conditions allows canceling the first part of (21) for $\lambda_n \neq \lambda$:

$$\int_0^{l_3} \sum_{\lambda_n \neq \lambda} \left\{ \begin{array}{c} C_{kn} C_k A_k \sin(\lambda_n x + \varphi_{kn}) \\ \cdot \sin(\lambda x + \varphi_k) \end{array} \right\} dx = 0 \qquad (22)$$

The other part of (21) is equivalent to:

$$\int_0^{l_3} \left\{ C_k^2 A_k \sin^2(\lambda x + \varphi_k) \right\} dx =$$
$$\frac{1}{2} (C_h^2 A_h l_h + C_c^2 A_c l_c + C_f^2 A_f l_f) \qquad (23)$$

Introducing (21), (22) and (23), equation (19) becomes:

$$\int_0^{l_3} \left\{ C_k A_k \left(T_{k_0}(x) - T_{k_{ss}}(x) \right) \sin(\lambda x + \varphi_k) \right\} dx$$
$$= \frac{1}{2} (C_h^2 A_h l_h + C_c^2 A_c l_c + C_f^2 A_f l_f). \qquad (24)$$

Applying integration by parts two times to the first part in (24) and considering boundary and continuity conditions, the first part in (24) becomes:

$$\int_0^{l_3} \left\{ C_k A_k \left(T_{k_0}(x) - T_{k_{ss}}(x) \right) \sin(\lambda x + \varphi_k) \right\} dx$$
$$= \frac{1}{\lambda^2} \int_0^{l_3} \left\{ \begin{array}{c} C_k A_k \frac{d^2}{dx^2} \left(T_{k_0}(x) - T_{k_{ss}}(x) \right) \\ \cdot \sin(\lambda x + \varphi_k) \end{array} \right\} dx \qquad (25)$$

Equations (24) or/and (25) allow defining the value of the unknown constant for a determined initial temperature distribution. In the case of an initial uniform distribution of temperature, $\frac{d^2}{dx^2} \left(T_{k_0}(x) - T_{k_{ss}}(x) \right)$ is equivalent to:

$$\left\{ \frac{d^2}{dx^2} \left(T_{k_0}(x) - T_{k_{ss}}(x) \right) = -\frac{I^2 \rho_0}{K_p A_k^2} \right\} \qquad (26)$$

In result, the integral in (24) is equivalent to:

$$\int_0^{l_3} \left\{ C_k A_k \left(T_{k_0}(x) - T_{k_{ss}}(x) \right) \sin(\lambda x + \varphi_k) \right\} dx$$
$$= \frac{I^2 \rho_0}{\lambda^3 K_p} \begin{bmatrix} -\frac{C_h}{A_h} \cos(\varphi_h) \\ +C_h A_h \cos(\lambda l_1 + \varphi_h) \left(\frac{1}{A_h^2} - \frac{1}{A_c^2} \right) \\ +C_c A_c \cos(\lambda l_2 + \varphi_c) \left(\frac{1}{A_c^2} - \frac{1}{A_f^2} \right) \\ +\frac{C_f}{A_f} \cos(\lambda l_3 + \varphi_f) \end{bmatrix} \qquad (27)$$

where I is the electrical current.

Combining (24) and (27) allows obtaining the value of the unknown constant C_h with respect to the actuator dimensions, material properties and the corresponding λ, φ_k and C_k:

$$C_h = \frac{2I^2 \rho_0}{\lambda^3 K_p \left(l_h + l_c \frac{A_c}{A_h} (\frac{C_c}{C_h})^2 + l_f \frac{A_f}{A_h} (\frac{C_f}{C_h})^2 \right)}$$
$$\cdot \begin{bmatrix} -\frac{1}{A_h^2} \cos(\varphi_h) \\ + \cos(\lambda l_1 + \varphi_h) \left(\frac{1}{A_h^2} - \frac{1}{A_c^2} \right) \\ + \frac{A_c}{A_h} \frac{C_c}{C_h} \cos(\lambda l_2 + \varphi_c) \left(\frac{1}{A_c^2} - \frac{1}{A_f^2} \right) \\ + \frac{1}{A_h A_f} \frac{C_f}{C_h} \cos(\lambda l_3 + \varphi_f) \end{bmatrix} \qquad (28)$$

Consequently, the solution of the electrothermal problem is obtained. The expression of the temperature with respect to time t and position x in the case of the actuator is as follows:

$$\left\{ \begin{array}{c} T_k(x,t) = T_{kss}(x) \\ + \sum_{n=1}^{\infty} C_{kn} \sin(\lambda_n x + \varphi_{kn}) e^{-\alpha_p \lambda_n^2 t} \end{array} \right\} \qquad (29)$$

The steady state temperature distribution $T_{kss}(x)$ is obtained in (5). The values of λ_n are calculated from (11) and the corresponding constants C_{kn} and φ_{kn} are obtained in (16), (17) and (28).

The obtained expression (29) allows obtaining directly the evolution of the temperature distribution inside U-shaped actuators with determined dimensions and material properties. In addition, this expression allows identifying the influence of all dimensions and parameters on the evolution of the temperature distribution inside the actuator.

3. Thermo-mechanical model

In this section, the displacement at the tip of the actuator is calculated based on the superposition and virtual work principles. The displacement is seen as an image of the evolution of the thermal distribution inside the actuator.

Generally, in micro-structures, the natural frequency is higher. In addition, simulations and experiments showed that the natural frequency of the actuator is of several KHz, which implies that the structural dynamic response is much faster then the electrothermal dynamic response (The dynamic response is shown

6

later in Section 4). Thus, the mechanical inertia is considered to be quasi-static.

The structure of the actuator allows amplifying the thermal expansion difference between the two sides of the actuator. Thermal expansion of each arm occurs due to temperature rise with respect to the following equation:

$$\Delta l = \int_0^l \alpha \left(T(x) - T_0 \right) dx \qquad (30)$$

Where Δl is the length expansion and α is the thermal expansion coefficient.

Figure 3 shows the surface forces N and moments M in the actuator anchored at the flexure after applying virtual unit forces and moments at the free border of the hot arm and at the tip of the actuator.
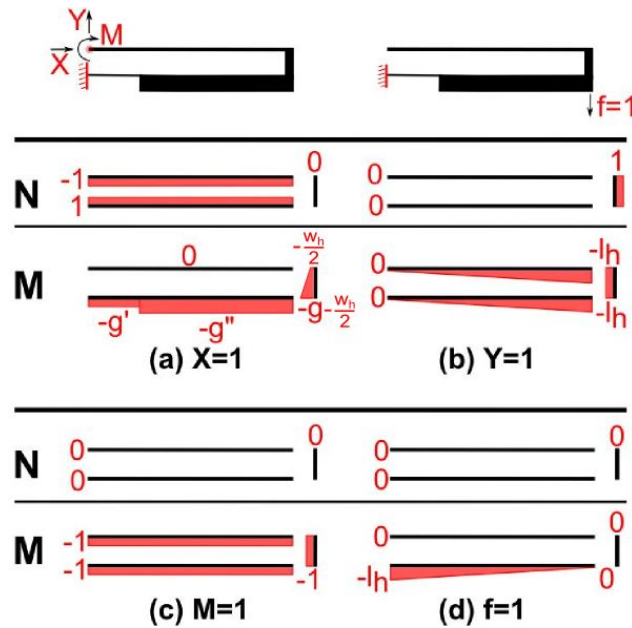
Figure 3. Surface forces N and moments M in the actuator anchored at the flexure after applying virtual forces and moment at the free border of the hot arm, (a), (b) and (c), and at the tip of the actuator (d).

The efforts X, Y and M are calculated in order to cancel the displacement and rotation at the free border of the hot arm as follows:

$$\begin{pmatrix} \delta_{XX} & \delta_{XY} & \delta_{XM} \\ \delta_{YX} & \delta_{YY} & \delta_{YM} \\ \delta_{MX} & \delta_{MY} & \delta_{MM} \end{pmatrix} \begin{pmatrix} X \\ Y \\ M \end{pmatrix} = \begin{pmatrix} \Delta \\ 0 \\ 0 \end{pmatrix} \qquad (31)$$

where $\Delta = \Delta L_h - \Delta L_c - \Delta L_f$.

The displacements and rotations after applying unit forces and moments $\delta_{XX}, \delta_{XY}...$ are obtained by applying the virtual works principle with respect to the

following equation:

$$\delta_{12} = \int_0^l \left(\frac{N_1 N_2}{EA} + \frac{M_1 M_2}{EI_y} \right) dx \qquad (32)$$

δ_{12}: Displacement or rotation in the direction of the virtual unit effort 1 after applying the real effort 2.
N_1: Surface forces with the virtual effort.
N_2: Surface forces with the real effort.
M_1: Bending moments with the virtual effort.
M_2: Bending moments with the real effort.
$I_y = \frac{bw^3}{12}$: Second moment of area of section with respect to the midline.
E: Young's modulus.

Based on (32), expressions of δ coefficients in (31) are as follows:

$$\delta_{XX} = \frac{g'^2 l_f}{EI_{yf}} + \frac{g''^2 l_c}{EI_{yc}} + \frac{2g^3 + 3gw_h(g + \frac{w_h}{2})}{6EI_{yg}} \\ + \frac{l_f}{ES_f} + \frac{l_c}{ES_c} + \frac{l_h}{ES_h} \qquad (33a)$$

$$\delta_{YY} = \frac{l_f^3}{3EI_{yf}} + \frac{l_h^3 - l_f^3}{3EI_{yc}} + \frac{gl_h^2}{EI_{yg}} + \frac{l_h^3}{3EI_{yh}} + \frac{g}{ES_g} \qquad (33b)$$

$$\delta_{MM} = \frac{l_f}{EI_{yf}} + \frac{l_c}{EI_{yc}} + \frac{g}{EI_{yg}} + \frac{l_h}{EI_{yh}} \qquad (33c)$$

$$\delta_{XY} = \delta_{YX} = \frac{g' l_f^2}{2EI_{yf}} + \frac{g''(l_h^2 - l_f^2)}{2EI_{yc}} \\ + \frac{g^2 l_h + l_h g w_h}{2EI_{yg}} \qquad (33d)$$

$$\delta_{XM} = \delta_{MX} = \frac{g' l_f}{EI_{yf}} + \frac{g'' l_c}{EI_{yc}} + \frac{g(g + w_h)}{2EI_{yg}} \qquad (33e)$$

$$\delta_{YM} = \delta_{MY} = \frac{l_f^2}{2EI_{yf}} + \frac{l_h^2 - l_f^2}{2EI_{yc}} + \frac{gl_h}{EI_{yg}} + \frac{l_h^2}{2EI_{yh}} \qquad (33f)$$

given that:
g: Gap width
g': Distance between hot arm and flexure mid-lines; $g' = g + \frac{w_h + w_f}{2}$
g'': Distance between hot and cold arm mid-lines; $g'' = g + \frac{w_h + w_c}{2}$

Calculation of the anchor efforts (31) allowed computing the surface forces and bending moments after the thermal expansion and then computing the displacement d at the tip of the actuator:

$$d = \frac{M + g'X}{2EI_{yf}} \left(2l_h l_f - l_f^2 \right) \\ + \frac{M + g''X}{2EI_{yc}} \left(2l_h l_c - l_h^2 + l_f^2 \right) \\ + Y \left(\frac{3l_h l_f^2 - 2l_f^3}{6EI_{yf}} + \frac{l_h^3 - 3l_h l_f^2 + 2l_f^3}{6EI_{yc}} \right) \qquad (34)$$

The analytical expression of the displacement d (34) shows that the displacement is directly

proportional to the expansion difference between two sides of the actuator.

$$d = k\Delta \tag{35}$$

4. Simulations, Experiments and discussion

The analytical models in this section are compared with FEM simulations and experiments and the evolution of the physical aspects (such as the temperature distribution and displacement) is discussed.

Analytical models, FEM simulations and experiments are run on a doped silicon U-shaped actuator with the dimensions shown in figure 4. These dimensions are chosen to provide the required performance for our microrobotic application [7].
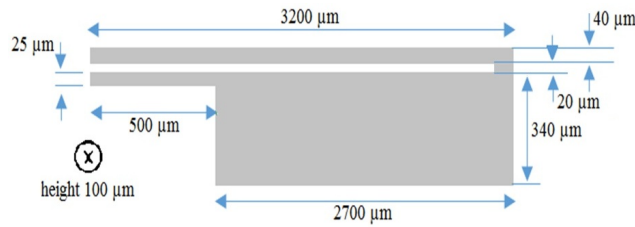
Figure 4. The modeled actuator dimensions

Most of the physical properties of doped silicon are dependent of the temperature and the doping concentration. The thermal conductivity K_p of silicon decreases with temperature [25]. It also decreases for thin layers and for high impurity concentration [26]. The specific heat C_p of silicon increases with temperature [27]. The electrical resistivity ρ_0 of silicon is also thermally dependent, its evolution with doping concentration and temperature is clarified in [28].

A simplifying assumption considering a constant value for these properties is taken. This hypothesis allows using the analytical solution of the electrothermal model to simulate the temperature distribution in the actuator.

Figure 5 shows evolution of the temperature distribution, at several instants between 0 and 1s, after applying a voltage of 15V at the anchors.

The electrothermal response is calculated directly from the analytical expression of $T(x, t)$ in (29). The physical properties used in the calculation have the following values: $T_s = 298.15\ K$, $\rho_d = 2330\ kg/m^3$, $C_p = 712\ J/K \cdot kg$, $K_p = 149\ W/mK$, $\rho_0 = 0.265\ \Omega mm$.

Different rates of temperature evolution in the three arms of the actuator are observed in figure 5. Further, figure 6 shows evolution of the average temperature of the hot arm, cold arm and flexure regarding the time.

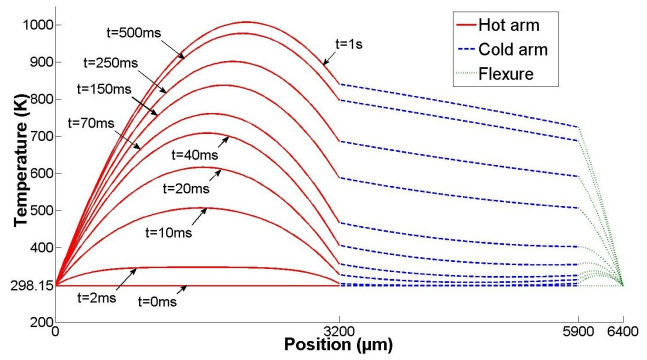Due to the lower width, the local Joule heating is higher in the flexure at the beginning. Thus, the

Figure 5. Temperature profiles in the actuator obtained analytically at 0, 2, 10, 20, 40, 70, 150, 250, 500 and 1000ms after applying 15V.
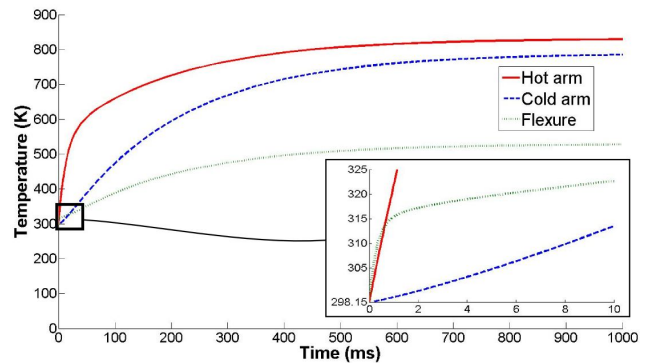
Figure 6. Evolution of the average temperature with time in the three arms of the actuator after applying 15V voltage.

initial temperature evolution is faster in the flexure, than in the hot and cold arms respectively. However, the temperature evolution rate of the flexure is limited by the cold temperature of the anchor and the cold arm and its evolution rate starts to slow down (zoom in figure 6) consequently. From the beginning, the temperature in the hot arm grows rapidly and despite a larger width than the flexure arm, the temperature in the hot arm becomes quickly higher. After around 100 ms, the temperature in the hot arm is closer to the steady state and its evolution rate becomes highly reduced whereas the temperatures in the cold and the flexure arms continue to rise until their steady state.

In result, the evolution rate of the temperature in the hot arm is higher than the cold side (cold and flexure arms) at the beginning while it is slower while getting closer to the steady state. This difference in the evolution rate is the reason behind the overshoot behavior of the actuator displacement shown later in this paper (figure 10), where the thermal expansion in each side is related to the temperature distribution (30) and the displacement is an image of the expansion difference (35).

A 3D FEM modeling is made using ANSYS and allows simulating the thermal distribution and the

8

structural deformation of the actuator after applying electrical voltage. The element used in the simulation SOLID226 is selected to allow a thermal-electric-structural analysis. The actuator in the simulation has the same dimensions as in figure 4. Convection and radiation are neglected and the physical properties and boundary conditions are the same as in the analytical modeling.

The evolution of the average temperature in the hot arm is considered as a comparison parameter of the electrothermal response between the analytical solution and FEM simulation. The comparison is shown in figure 7 for two applied voltages (15 and 18V).
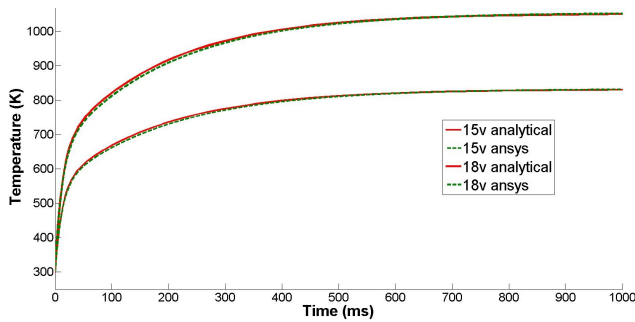
Figure 7. Comparison between the analytical model and ANSYS for the evolution of the average temperature in the hot arm.

Figure 7 shows a very good agreement between the presented electrothermal solution and FEM simulations. The temperature distribution in the 3D FEM simulation is remarked to be homogeneous in the cross section along each arm while it is slightly non-homogeneous at the borders. This validates the one-dimensional simplifying assumption used in the electrothermal analytical model.

Experiments that are run on microfabricated actuators allowed us to record the displacement of the actuator with a high speed camera after applying electrical voltages.

The actuators are fabricated using single-crystalline silicon-on-insulator (SOI) wafer, with a $100\mu m$ device layer, a $2\mu m$ buried oxide (SiO_2) and a $380\mu m$ handle layer. The device layer with a <1-0-0> orientation is highly doped p-type and has a range of resistivity of $0.1 - 0.3\ \Omega mm$.

The shape of the actuator after fabrication is shown in figure 8. The active parts of the actuator are realized in the device layer while the handle layer serves as a support of the whole device. The intermediate SiO_2 layer is an electrical insulator, it allows separating the anchor pads electrically.

In the experiments, the actuators on wafer are placed in a micromanipulation station under a high speed camera. This camera allows recording the displacement of the actuator throughout a microscope
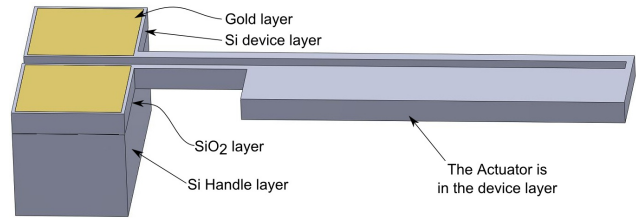

Figure 8. Layers of the microfabricated actuator.

with a frame rate of up to several ten thousands of frames per second. The electrical connection with the actuator is provided with 2 conductive probes that are connected to the actuator pads. The displacement of the actuator after applying a step voltage is recorded on videos. Figure 9 shows two frames of an experience video in the on and off state respectively. The displacement is then measured directly on the videos using a specific software. For example, the measured displacement in figure 9.b is around $150\mu m$.
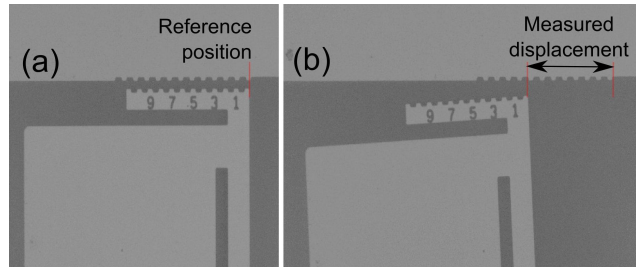

Figure 9. Frames from an experience video on the actuator, at the rest position (a) and during displacement (b).

Figure 10 shows the displacement curves of the actuator with respect to time obtained from the analytical models, FEM simulations and experiments. Displacement curves are shown for two applied voltages (15V and 18V).
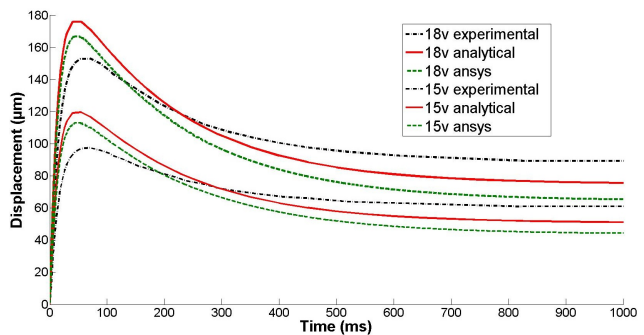

Figure 10. Comparison between the analytical model, ANSYS and experiments for the displacement curves at the tip of the actuator.

Noting that the expansion coefficient α is considered to be thermally dependent in the analytical calculation (30) and FEM simulations. This consideration

was taken into account because of the large variation of the expansion coefficient of silicon with temperature (from $2.568\mu m/mK$ at $300K$ to $4.258\mu m/mK$ at $1000K$). Yokada et al. in [29] have defined an equation for the thermal expansion coefficient of silicon with respect to temperature:

$$\alpha = 10^{-6} \left(\begin{array}{c} 3.725 \left(1 - e^{-5.88\cdot 10^{-3}(T-124)}\right) \\ +5.548 \cdot 10^{-4}T \end{array} \right) \quad (36)$$

Figure 10 shows an important overshoot of displacement of the actuator before reaching a steady state position. The transient shape of displacement is due to the variation of the evolution rate of temperature distribution on the two sides of the actuator as shown in figures 5 and 6.

Fig 10 shows that this behavior of displacement is common between the analytical models, FEM simulations and experiments but with slight differences.

The displacement curves of the analytical models and the FEM simulation have the same shapes but with a small shift between the two theoretical curves. Consequently, as there's a good agreement in terms of the electrothermal response as shown in figure 7 and as the displacement is equivalent to the expansion difference (35) which is an image of the temperature distribution, then the difference in the calculated displacement returns mostly to the thermo-mechanical model. This difference may return to the negligence of the shear force and the one dimensional simplification in the analytical calculation. The different arms in the actuator are considered as lines and there is an uncertainty in the calculation particularly at the connection between arms. In addition, the slightest difference in the electrothermal model is amplified in the displacement calculation due to the amplifying effect of the structure.

In the other side, there is a difference in the shape of the displacement curves between the calculated and experimental results as shown in figure 10. Experiments show a lower overshoot and a higher steady state final position. This difference may exist due to the assumptions taken in the calculation (negligence of convection and radiation, boundary conditions etc.), the uncertainty in the physical properties and the thermal dependence of the physical properties of silicon especially in the steady state where the actuator is overheated.

In result, the analytical models presented in this paper show good agreement with the results of the FEM simulations and experiments. An almost perfect agreement is noted in terms of the transient electrothermal response between the analytical solution and FEM simulations despite the 1D simplification of the analytical model.

Less agreement is noted in the calculated displacement. A small shift between the displacement curves is noted with the FEM simulation results and a slight difference in the shape of these curves is noted with the experimental results.

Originality of the electrothermal analytical model is that it provides an exact solution of the hybrid PDEs that describe the electrothermal behavior of the three arms of the actuator. The calculation method can be extended to any number of connected hybrid PDEs and evidently for other defined boundary conditions. The cooling cycle can be modeled also using the analytical modeling by canceling the Joule heating term in the electrothermal equation and introducing the final temperature distribution in the heating cycle as the initial temperature distribution in the cooling cycle.

The importance of the analytical models is not only that they provide a solution for an equation. The obtained expressions show clearly the influence of the different dimensions and material properties on the electrothermal behavior and the displacement of the actuator. These expressions can be used to design and optimize the dimensions and behavior of the U-shaped actuator.

5. Conclusion

In this paper, a complete electro-thermo-mechanical analytical modeling of the dynamic behavior of U-shaped electrothermal actuators was presented. The problem was treated by a sequence of two analytical models: electro-thermal and thermo-mechanical. The first one concerns the computation of the evolution of the thermal distribution in the actuator, while the second one allows computing the displacement resulting from the thermal distribution.

The electrothermal model provided an exact solution of the hybrid PDEs that describe the electrothermal behavior in the three arms of the actuator. The relation between the displacement and the thermal distribution is then provided in the thermo-mechanical model. FEM simulations and experiments were run on doped silicon actuators. the analytical models showed a good agreement with the results of the FEM simulation and experiments in terms of the thermal distribution and the displacement.

The presented modeling opens up important perspectives in terms of the modeling, design and optimization of the actuator. For the modeling, several development axes are possible such as the modeling of the cooling cycle, free and charged displacements with external forces, consideration of phenomena neglected in the present approach (convection or radiation, different boundary conditions, temperature dependence of the properties, etc). In the other side, the influence of the different dimensions and properties

10

on the electrical, thermal and mechanical behavior of the actuator can be concluded from the presented analytical expressions which is very important for the design and optimization.

Acknowledgment

References

[1] Edward S Kolesar, Peter B Allen, Jeffery T Howard, Josh M Wilken, and Noah Boydston. Thermally-actuated cantilever beam for achieving large in-plane mechanical deflections. *Thin Solid Films*, 355:295–302, 1999.

[2] H Guckel, J Klein, T Christenson, K Skrobis, M Laudon, and EG Lovell. Thermo-magnetic metal flexure actuators. In *Solid-State Sensor and Actuator Workshop, 1992. 5th Technical Digest., IEEE*, pages 73–75. IEEE, 1992.

[3] John H Comtois and Victor M Bright. Applications for surface-micromachined polysilicon thermal actuators and arrays. *Sensors and Actuators A: Physical*, 58(1):19–25, January 1997.

[4] Timothy Moulton and GK Ananthasuresh. Micromechanical devices with embedded electro-thermal-compliant actuation. *Sensors and Actuators A: Physical*, 90(1):38–48, 2000.

[5] S-C Chen and Martin L Culpepper. Design of contoured microscale thermomechanical actuators. *Microelectromechanical Systems, Journal of*, 15(5):1226–1234, 2006.

[6] V. Chalvet, Y. Haddab, and P. Lutz. A microfabricated planar digital microrobot for precise positioning based on bistable modules. Early Access Online, 2013.

[7] Hussein Hussein, Vincent Chalvet, Patrice Le Moal, Gilles Bourbon, Yassine Haddab, and Philippe Lutz. Design optimization of bistable modules electrothermally actuated for digital microrobotics. In *Advanced Intelligent Mechatronics (AIM), 2014 IEEE/ASME International Conference on*, pages 1273–1278. IEEE, 2014.

[8] Zhenlu Wang, Xuejin Shen, and Xiaoyang Chen. Design, modeling, and characterization of a mems electrothermal microgripper. *Microsystem Technologies*, pages 1–8, 2015.

[9] Qing-An Huang and Neville Ka Shek Lee. Analysis and design of polysilicon thermal flexure actuator. *J. Micromech. Microeng.*, 9(1):64, March 1999.

[10] Y. Kuang, Q.-A. Huang, and N. K. S. Lee. Numerical simulation of a polysilicon thermal flexure actuator. *Microsystem Technologies*, 8(1):17–21, March 2002.

[11] R. Hickey, M. Kujath, and T. Hubbard. Heat transfer analysis and optimization of two-beam microelectromechanical thermal actuators. *Journal of Vacuum Science & Technology A*, 20(3):971–974, 2002.

[12] Sylvaine Muratet. *Conception, caractérisation et modélisation: Fiabilité prédictive de MEMS à actionnement électrothermique*. PhD thesis, INSA de Toulouse, 2005.

[13] Mohammad Mayyas, Panos S Shiakolas, Woo Ho Lee, and Harry Stephanou. Thermal cycle modeling of electrothermal microactuators. *Sensors and Actuators A: Physical*, 152(2):192–202, 2009.

[14] Ph Lerch, C Kara Slimane, Bartlomiej Romanowicz, and Ph Renaud. Modelization and characterization of asymmetrical thermal micro-actuators. *Journal of Micromechanics and Microengineering*, 6(1):134, 1995.

[15] RRA Syms. Long-travel electrothermally driven resonant cantilever microactuators. *Journal of Micromechanics and Microengineering*, 12(3):211, 2002.

[16] Ryan Hickey, Dan Sameoto, Ted Hubbard, and Marek Kujath. Time and frequency response of two-arm micromachined thermal actuators. *Journal of Micromechanics and Microengineering*, 13(1):40, 2002.

[17] Vincent A Henneken, Marcel Tichem, and Pasqualina M Sarro. Improved thermal u-beam actuators for micro-assembly. *Sensors and Actuators A: Physical*, 142(1):298–305, 2008.

[18] Hussein Hussein, Patrice Le Moal, Gilles Bourbon, Yassine Haddab, and Philippe Lutz. Analysis of the dynamic behavior of a doped silicon u-shaped electrothermal actuator. In *Advanced Intelligent Mechatronics (AIM), 2015 IEEE/ASME International Conference on*. IEEE, 2015.

[19] Liwei Lin and Mu Chiao. Electrothermal responses of lineshape microstructures. *Sensors and Actuators A: Physical*, 55(1):35–41, 1996.

[20] Q.-A. Huang and N. K. S. Lee. Analytical modeling and optimization for a laterally-driven polysilicon thermal actuator. *Microsystem Technologies*, 5(3):133–137, February 1999.

[21] Eniko T Enikov, Shantanu S Kedar, and Kalin V Lazarov. Analytical model for analysis and design of v-shaped thermal microactuators. *Microelectromechanical Systems, Journal of*, 14(4):788–798, 2005.

[22] Alain Jungen, Marc Pfenninger, Marc Tonteling, Christoph Stampfer, and Christofer Hierold. Electrothermal effects at the microscale and their consequences on system design. *Journal of Micromechanics and Microengineering*, 16(8):1633, 2006.

[23] Ozgur Ozsun, B Erdem Alaca, Arda D Yalcinkaya, Mehmet Yilmaz, Michalis Zervas, and Yusuf Leblebici. On heat transfer at microscale with implications for microactuator design. *Journal of Micromechanics and Microengineering*, 19(4):045020, 2009.

[24] Ryan Hickey, Marek Kujath, and Ted Hubbard. Heat transfer analysis and optimization of two-beam microelectromechanical thermal actuators. *Journal of Vacuum Science Technology A: Vacuum, Surfaces, and Films*, 20(3):971–974, 2002.

[25] CJ Glassbrenner and Glen A Slack. Thermal conductivity of silicon and germanium from 3 k to the melting point. *Physical Review*, 134(4A):A1058, 1964.

[26] M Asheghi, K Kurabayashi, R Kasnavi, and KE Goodson. Thermal conduction in doped single-crystal silicon films. *Journal of Applied Physics*, 91(8):5079–5088, 2002.

[27] A. S. Okhotin, A. S. Pushkarskij, and V. V. Gorbachev. Thermophysical properties of semiconductors. 1972.

[28] Sheng S Li. The dopant density and temperature dependence of hole mobility and resistivity in boron doped silicon. *Solid-State Electronics*, 21(9):1109–1117, 1978.

[29] Yasumasa Okada and Yozo Tokumaru. Precise determination of lattice parameter and thermal expansion coefficient of silicon between 300 and 1500 k. *Journal of applied physics*, 56(2):314–320, 1984.

Appendix A. Lineshaped beam electrothermal response

In this appendix, we recall the calculation method of the electrothermal response for a lineshaped microbeam. Considering a constant temperature at the borders and an initial distribution of the temperature as follows:

$$T(0,t) = T(l,t) = T_\infty$$
$$T(x,0) = T_0(x) \tag{A.1}$$

Where l is the length of the beam.

Introducing the boundary conditions in (1), the steady state temperature in the lineshaped beam has the following distribution:

$$T_{ss}(x) = -\frac{J^2\rho_0}{2K_p}x^2 + \frac{J^2\rho_0}{2K_p}lx + T_\infty \tag{A.2}$$

In order to obtain the transient solution, the temperature is decomposed in two parts:

$$T(x,t) = u(x) + v(x,t) \tag{A.3}$$

Where $u(x)$ is the steady state solution $u(x) = T_{ss}(x)$.

This decomposition allows assigning to zero the boundary conditions of $v(x,t)$. The boundary and initial conditions for $v(x,t)$ are as follows:

$$v(0,t) = v(l,t) = 0$$
$$v(x,0) = T_0(x) - T_{ss}(x) \tag{A.4}$$

Introducing (A.3) in the electrothermal equation (1), the PDE of $v(x,t)$ can be written as follows:

$$\frac{\partial^2 v}{\partial x^2} = \frac{1}{\alpha_p}\frac{\partial v}{\partial t} \tag{A.5}$$

Where $\alpha_p = \frac{K_p}{\rho_d C_p}$ is the thermal diffusivity.

Using the method of separation of variables (Fourier method), $v(x,t)$ can be decomposed in two functions with separated variables:

$$v(x,t) = X(x)\Gamma(t) \tag{A.6}$$

Introducing the separated functions (A.6) in the PDE (A.5) allows obtaining the PDEs of $\Gamma(t)$ and $X(x)$:

$$\begin{cases} \dfrac{\partial \Gamma}{\partial t} + \alpha_p\lambda^2\Gamma = 0 \\ \dfrac{\partial^2 X}{\partial x^2} + \lambda^2 X = 0 \end{cases} \tag{A.7}$$

where λ is a positive non-zero constant assigned to $X(x)$ and $\Gamma(t)$.

The general solutions of $\Gamma(t)$ and $X(x)$ have the following forms:

$$\begin{cases} \Gamma(t) = e^{-\alpha_p\lambda^2 t} \\ X(x) = a\sin(\lambda x) + b\cos(\lambda x) \end{cases} \tag{A.8}$$

where a, b and λ are the unknowns.

Introducing the boundary conditions, we conclude that the unknowns have infinity of solutions with a periodic form: $a = a_n$, $b = b_n$ and $\lambda = \lambda_n$, where n is a positive integer. In result, according to the superposition principle:

$$v(x,t) = \sum_{n=1}^{\infty} X_n(x)\Gamma_n(t) \tag{A.9}$$

where X_n and Γ_n are equivalent to X and Γ respectively for $a = a_n$, $b = b_n$ and $\lambda = \lambda_n$.

For the boundary conditions in A.1, the constants b_n and λ_n are equivalent to: $b_n = 0$, $\lambda_n = n\pi/l$. Afterwards, the transient solution of the temperature has the following form:

$$T(x,t) = T_{ss}(x) + \sum_{n=1}^{\infty} a_n \sin\left(\frac{n\pi}{l}x\right) e^{-\frac{\alpha_p n^2\pi^2}{l^2}t} \tag{A.10}$$

Introducing the initial temperature condition, we recognize a Fourier series form, enabling to determine the expression of a_n.

$$a_n = \frac{2}{l}\int_0^l (T_0(x) - T_{ss}(x))\sin\left(\frac{n\pi}{l}x\right) \tag{A.11}$$

Thereby, all the unknowns are determined and the solution is obtained.